

## Turbulence structures of wall-bounded shear flows found using DNS data

By M. S. CHONG<sup>1</sup>, J. SORIA<sup>2</sup>, A. E. PERRY<sup>1</sup>, J. CHACIN<sup>3</sup>,  
B. J. CANTWELL<sup>4</sup> AND Y. NA<sup>5</sup>

<sup>1</sup>Department of Mechanical and Manufacturing Engineering, University of Melbourne, Parkville, VIC 3052, Australia

<sup>2</sup>Department of Mechanical Engineering, Monash University, Clayton, VIC 3168, Australia

<sup>3</sup>Department of Mechanical Engineering, Stanford University, CA 94305, USA

<sup>4</sup>Department of Aeronautics and Astronautics, Stanford University, CA 94305, USA

<sup>5</sup>Department of Theoretical and Applied Mechanics, University of Illinois at Urbana-Champaign, IL 61801, USA

(Received 21 March 1997 and in revised form 10 October 1997)

This work extends the study of the structure of wall-bounded flows using the topological properties of eddying motions as developed by Chong *et al.* (1990), Soria *et al.* (1992, 1994), and as recently extended by Blackburn *et al.* (1996) and Chacin *et al.* (1996). In these works, regions of flow which are focal in nature are identified by being enclosed by an isosurface of a positive small value of the discriminant of the velocity gradient tensor. These regions resemble the attached vortex loops suggested first by Theodorsen (1955). Such loops are incorporated in the attached-eddy model versions of Perry & Chong (1982), Perry *et al.* (1986), and Perry & Marusic (1995), which are extensions of a model first formulated by Townsend (1976). The direct numerical simulation (DNS) data of wall-bounded flows studied here are from the zero-pressure-gradient flow of Spalart (1988) and the boundary layer with separation and reattachment of Na & Moin (1996). The flow structures are examined from the viewpoint of the attached eddy hypothesis.

---

### 1. Introduction

Townsend (1976) was the first to show by analysis how the properties of attached eddies and their distribution of scales affect the mean statistics of the flow. It is assumed that there exist an assemblage of attached eddies with a range of length scales and the characteristic length scale of a given eddy is proportional to the height it extends from the wall. These eddies were treated by Townsend as inviscid motions which convect with a ‘velocity of slip’ relative to the wall. This velocity of slip overcomes the condition of no-slip by the existence of a viscous sublayer. In the particular analysis of Townsend, the characteristic velocity scale of the eddies is taken to be the wall shear velocity. The analysis was simplified by assuming geometrical similarity in attached eddy shapes and it is felt that this is not too far from the truth and any departure will have only a weak effect on the final results. The analysis of Townsend has been extended in many stages by Perry & Abell (1977), Perry & Chong (1982), Perry, Henbest & Chong (1986), Perry, Li & Marusic (1991), Perry & Marusic (1995) and Marusic & Perry (1995) so that not only broadband intensity distributions are explained as was done by Townsend but also the mean flow and spectra can be

deduced from assumed scale distributions. If these various developments prove to be correct then there is the possibility that this will aid in producing more realistic models for engineering calculations of the streamwise growth and evolution of the various mean statistical quantities of turbulent boundary layers, e.g. see Perry *et al.* (1991), Perry, Marusic & Li (1994). Current models such as those based on  $k-\epsilon$  theories are controversial and are not universally accepted. One noteworthy feature of the attached eddy approach is that the Biot–Savart law and scale distributions give a connection between the mean vorticity distribution and the Reynolds shear stress distribution and this is an important ingredient in any closure scheme.

Townsend made no commitment regarding the actual eddy shapes. However, the vortex loop structures suggested by Theodorsen (1955) certainly fit the role of Townsend's attached eddies. The attached eddy hypothesis has recently been extended by Perry & Marusic (1995) and Marusic & Perry (1995) to include boundary layers developing in arbitrary pressure gradients and it was found necessary to introduce the concept of 'wall eddies' where the vortex cores extend to the wall and the 'wake eddies' which consist of spanwise undulating vortex cores which do not connect with the wall, and this fits in with the mean flow wall–wake model of Coles (1956). The establishment of the existence of these various structures is crucial to further developments. Unfortunately, at present the evidence for their existence is circumstantial, i.e. they can be used analytically for establishing a logarithmic defect law, a  $-1$  power spectral density for the streamwise velocity fluctuations and other observed properties and so their existence can be inferred but it is difficult to see these structures directly. Flow visualization helps in this regard but is difficult to interpret rigorously. This paper aims to provide some direct evidence using DNS data for both zero-pressure-gradient boundary layers and a layer which approaches separation, separates and then reattaches.

The vortex loops envisaged by Theodorsen (1955) and also by Head & Bandyopadhyay (1981) were inspired by flow visualization and are referred to by many names depending on the shape one believes they possess, e.g. horseshoes, hairpins,  $\cap$ ,  $\Lambda$  or  $\Pi$  eddies, etc. A problem immediately arises as to what constitutes a vortex core. There has been some debate regarding this over the years and many workers have been involved, e.g. Truesdell (1954), Cantwell (1979), Vollmers (1983), Dallman (1983), Chong, Perry & Cantwell (1989, 1990), Robinson (1991), Lugt (1979), Jeong & Hussain (1995), Perry & Chong (1994), and Soria & Cantwell (1994), to mention a few. To avoid endless discussion and debate the authors will simply identify those regions in the flow which are 'focal', to be defined shortly, and refer to them as 'focal regions'. The attached eddies postulated in the attached eddy hypothesis need not necessarily be focal since this condition depends on the relative strengths of the local rate-of-strain tensor and the local rate of rotation tensor (defined in (9) and (10) respectively). The results of the attached eddy hypothesis are derived purely from the Biot–Savart law and in no way depend on the above relative strengths. Whether or not a region of vorticity is focal depends on the rate-of-strain environment in which it is embedded and so also do all definitions of a vortex core. Nevertheless it is felt that most if not all of the attached eddies should display extensive focal regions as a result of the work of Blackburn, Mansour & Cantwell (1996), who examined the data from channel flow computations of Kim (1989). Here focal regions were found to exist in tubes, some of which extended from very close to the wall to the centreplane of the channel. The authors consider these to be the clearest and most spectacular indicators of eddying motions so far seen in DNS data and at first sight look like the attached eddies envisaged by Perry & Chong (1982).

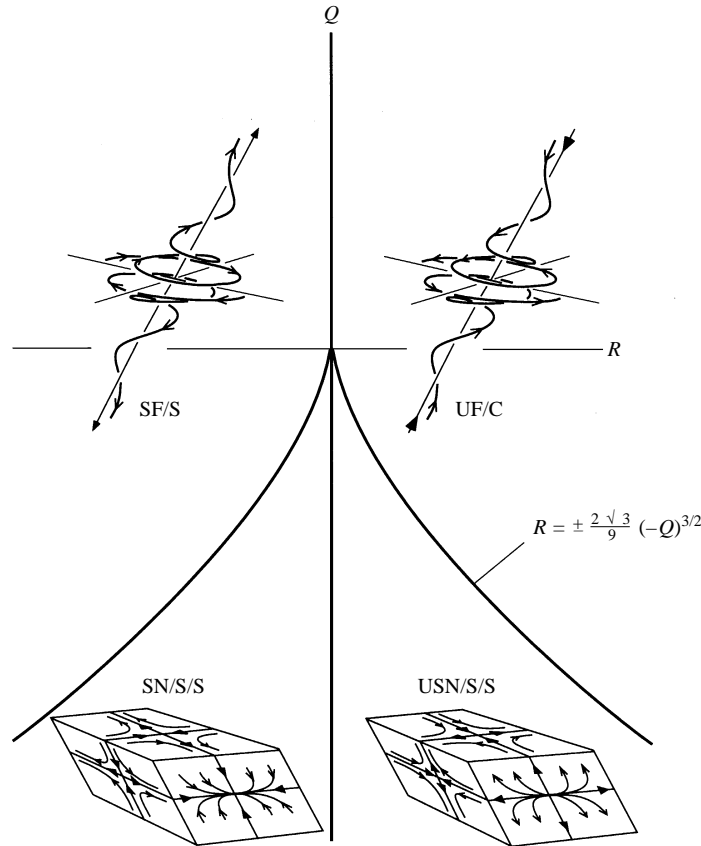


FIGURE 1. Local non-degenerate topologies in the  $(Q, R)$ -plane. SF/S: stable focus/stretching, UF/C: unstable focus/contracting, SN/S/S: stable node/saddle/saddle and USN/S/S: Unstable node/saddle/saddle.

Following Chong *et al.* (1989, 1990), the geometry of the streamline pattern close to and surrounding any point in the flow, as seen by a non-rotating observer moving with the velocity of that point, can be classified by studying certain invariants of the velocity gradient tensor  $A_{ij} = \partial u_i / \partial x_j$  at that point. Here  $u_i$  is the velocity vector and  $x_i$  is the space vector. The characteristic equation of  $A_{ij}$  is

$$\lambda^3 + P\lambda^2 + Q\lambda + R = 0, \tag{1}$$

where  $P$ ,  $Q$  and  $R$  are the tensor invariants. These are

$$P = -\text{tr}(\mathbf{A}) \tag{2}$$

$$Q = \frac{1}{2}(P^2 - \text{tr}(\mathbf{A}^2)) \tag{3}$$

and

$$R = -\det(\mathbf{A}). \tag{4}$$

For incompressible flow,  $P = 0$  from continuity and so

$$\lambda^3 + Q\lambda + R = 0. \tag{5}$$

The eigenvalues  $\lambda$  which determine the topology of the local flow pattern are

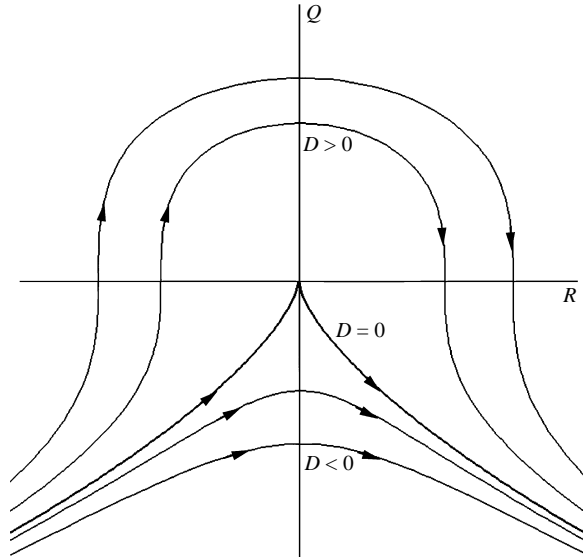


FIGURE 2. Trajectories of constant  $D$  on the  $(R, Q)$ -plane.

determined by the invariants  $R$  and  $Q$ . In fact the  $(R, Q)$ -plane, shown in figure 1, is divided into regions according to flow topology.

The discriminant of  $A_{ij}$  is defined as

$$D = \frac{27}{4}R^2 + Q^3 \tag{6}$$

and the boundary dividing flows with complex eigenvalues from those with all real eigenvalues is

$$D = 0. \tag{7}$$

Figure 2 shows contours of  $D$  on the  $(R, Q)$ -plane. For  $D > 0$ , (5) admits two complex and one real solution for  $\lambda$ . Such points are called foci and are part of the focal regions mentioned earlier. If  $D < 0$ , all three solutions for  $\lambda$  are real and the associated pattern is referred to as a node-saddle-saddle point according to the terminology adopted by Chong *et al.* (1990).

The velocity gradient tensor can be split into two components:

$$A_{ij} = S_{ij} + W_{ij}, \tag{8}$$

where  $S_{ij}$  is the symmetric rate of strain tensor and  $W_{ij}$  is the skew symmetric rate of rotation tensor. These are given by

$$S_{ij} = \frac{1}{2} \left( \frac{\partial u_i}{\partial x_j} + \frac{\partial u_j}{\partial x_i} \right) \tag{9}$$

and

$$W_{ij} = \frac{1}{2} \left( \frac{\partial u_i}{\partial x_j} - \frac{\partial u_j}{\partial x_i} \right). \tag{10}$$

The invariants of  $S_{ij}$  are  $P_s$ ,  $Q_s$ , and  $R_s$  and are defined in an analogous way to the invariants of  $A_{ij}$ . For incompressible flow  $P_s = 0$ ,

$$Q_s = -\frac{1}{2}S_{ij}S_{ij} \tag{11}$$

and

$$R_s = -\frac{1}{3}S_{ij}S_{jk}S_{ki}. \quad (12)$$

The corresponding invariants of  $W_{ij}$  are  $P_w$ ,  $Q_w$  and  $R_w$ .  $P_w = R_w = 0$  but  $Q_w$  is non-zero and is given by

$$Q_w = \frac{1}{2}W_{ij}W_{ij}, \quad (13)$$

which is proportional to the enstrophy density and is always positive. Another relation of interest is

$$\phi = 2\nu S_{ij}S_{ij} = -4\nu Q_s, \quad (14)$$

where  $\phi$  is the dissipation of kinetic energy into heat per unit mass and it should be noted that  $Q_s$  is always a negative quantity.

It can be shown that

$$Q = Q_w + Q_s = \frac{1}{2}(W_{ij}W_{ij} - S_{ij}S_{ij}). \quad (15)$$

According to the work of Vieillefosse (1982, 1984) and the more recent work of Cantwell (1992), the evolution of the velocity gradient tensor  $A_{ij}$  for a fluid particle is given by

$$\frac{dA_{ij}}{dt} + A_{ik}A_{kj} - A_{km}A_{mk} \frac{\delta_{ij}}{3} = H_{ij}. \quad (16)$$

Here  $d/dt$  is the total derivative,  $\delta_{ij}$  is the Kronecker delta and

$$H_{ij} = -\left(\frac{\partial^2 p}{\partial x_i \partial x_j} - \frac{\partial^2 p}{\partial x_k \partial x_k} \frac{\delta_{ij}}{3}\right) + \nu \frac{\partial^2 A_{ij}}{\partial x_k \partial x_k}. \quad (17)$$

If the viscous term and the pressure Hessian terms are small, the evolution of  $A_{ij}$  for fluid particles follows the so-called restricted Euler equation, and solution trajectories of such particles follow the contours of constant  $D$  on the  $(R, Q)$ -plane as shown in figure 2. It is thought that this might be an appropriate description of the motions for fine-scale eddies at high Reynolds numbers. It is found here that this restricted Euler equation is not valid for the Spalart (1988) dataset, which is of course at low Reynolds number. However, computations show that once a particle is focal it is highly probable that it will remain focal. This study of particle trajectories on the  $(R, Q)$ -plane gives us a first glimpse of how fluid dynamics might be combined with the usual kinematic description of eddy structures as has been used in the attached eddy hypothesis.

It has been pointed out that three-dimensional plots of vortex lines or particle trajectories are extremely complex and confusing and not very helpful in gaining an insight into eddying motions (Cantwell 1979). However, a very interesting feature of the isosurfaces of constant  $D$  found by Blackburn *et al.* (1996) is that they enclose a rather concentrated and well-ordered bundle of vortex lines. Finally, Blackburn *et al.* found that isosurfaces of constant  $D$  were superior to isosurfaces of enstrophy density or dissipation of kinetic energy for showing clear, well-defined structures. The authors do not fully understand why this should be and this is a question which needs to be pursued in future work.

## 2. Results

### 2.1. Normalization of the discriminant

The raw values of the discriminant  $D$  were used in the case of the Spalart DNS data without any additional normalization. In the case of the Na & Moin DNS

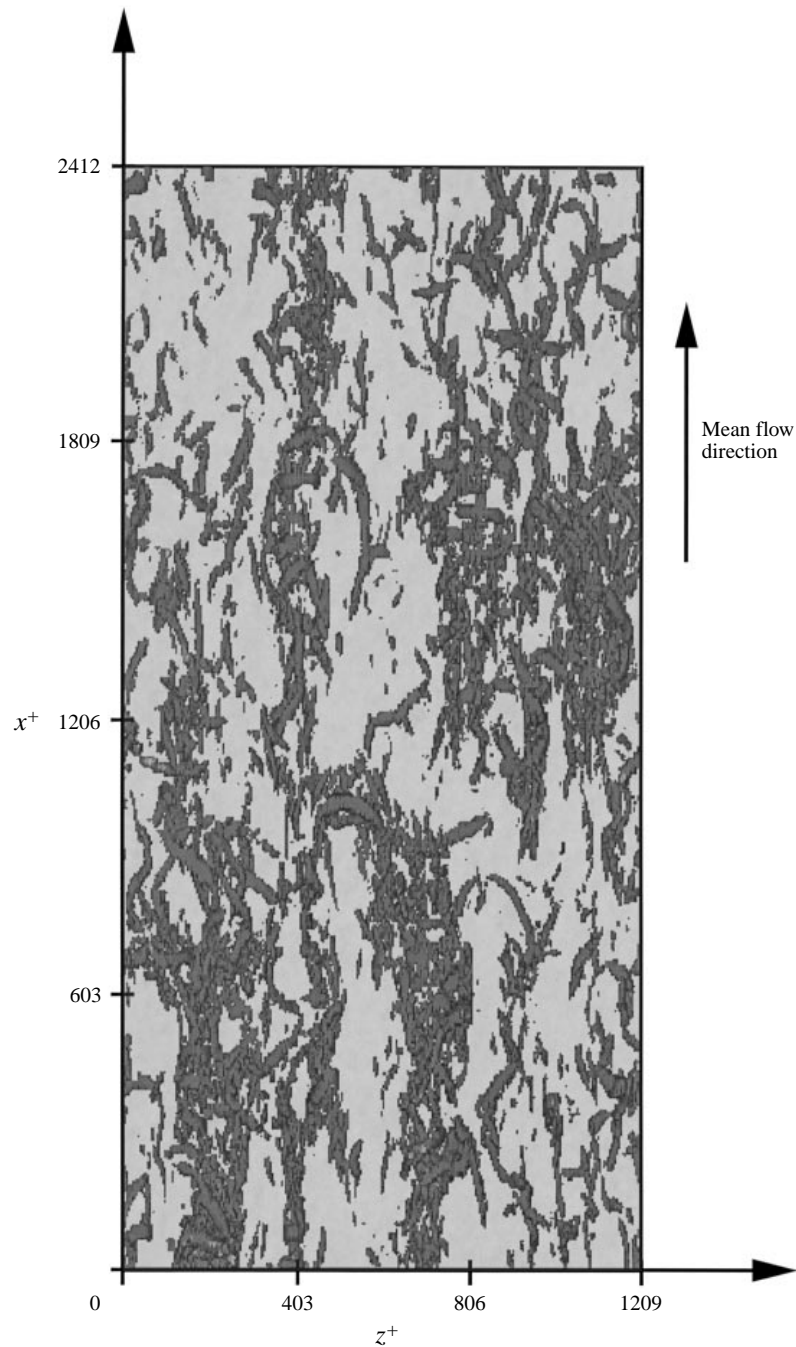


FIGURE 3. Isosurfaces of discriminant ( $D \approx 0$ ) for zero-pressure-gradient data of Spalart for  $Re_\theta = 670$  (from Chacin *et al.* 1996).

dataset, it is assumed that the inflow free-stream velocity is unity and that all length scales in the database are normalized by  $\delta_{in}^*$ , the displacement thickness of the inflow boundary layer. The computed raw values of  $D$  were normalized by a velocity gradient representative of the mean separation bubble flow to the power of 6. This resulted in

the raw values of  $D$  being multiplied by a factor of  $10^6$ , and so maximum values of normalized  $D$  were of order  $10^6$ . Typical values of  $D$  used in its isosurface visualization were of the order of 1–10.

## 2.2. Zero-pressure-gradient boundary layer

Figure 3 shows a clear picture (from Chacin, Cantwell & Kline 1996) of isosurfaces of the discriminant for part of the data of Spalart (1988) for a zero-pressure-gradient turbulent boundary layer at  $Re_\theta = 670$ . Some Theodorsen-type vortices are apparent together with intertwining tubes forming braids which are near the surface and are aligned in the streamwise direction. Figure 4(a–c) shows the same flow case of Spalart but for a different time frame covering a larger field of data. The figures are ordered in diminishing values of  $D$ . Figure 4(a) shows structures which could be interpreted as  $\cap$  or  $\Lambda$  eddies when viewed from upstream. These loops appear to lean in the streamwise direction. As the ‘threshold’ is reduced (i.e. as the value of  $D$  for the isosurface is reduced), more attached vortex loops become apparent, but the picture becomes confusing. The structures are not as smooth as the Chacin *et al.* (1996) data, and this is because of computer storage problems for the graphical visualization. There is nonetheless a suggestion of Theodorsen-type structures with focal tubes coming down to the wall and running along it in the negative streamwise direction. Superposition of vortex lines (done at the computer terminal) is confusing, but they tend to loop and lean in the streamwise direction in a manner similar to the isosurfaces of  $D$ .

Particle migration on the  $(R, Q)$ -plane shows that there is a rapid convergence to small but positive  $D$ . Figure 5 shows a typical calculation for a selection of particles with  $D > 0$  at the initial time. These particles are identified at  $t = 0$  and then followed in space as the DNS code is run forward in time for several eddy characteristic turnover times. These calculations show that once a particle has a positive discriminant (i.e. once it is focal), it has a high probability of remaining focal over several eddy turnover times. Various models for the  $H_{ij}$  term are currently being formulated. One recent model by Martin & Dopazo (1995) shows ensemble-averaged  $(R, Q)$ -trajectories with the topology sketched in figure 6, and this is consistent with the above findings. Time evolution computations and animations of the isosurfaces of the discriminant show that such surfaces retain their shape and identity for considerable streamwise distances. When viewing a movie made up of successive frames, these structures appear to convect downstream in close accordance with Taylor’s hypothesis. Some frames from the movie are shown in figure 7. Smaller structures close to the wall appear to be convecting at smaller velocities than the larger structures further away from the wall. All of this is consistent with aspects of the attached eddy model discussed by Perry *et al.* (1986).

In zero-pressure-gradient layers, there seems to be a strong link between these attached eddies and the Reynolds shear stress. Perry & Chong (1982) showed that it is likely that they contribute almost entirely to the mean vorticity distribution and the Reynolds shear stress distribution. Figure 8 shows that peaks in the time-averaged values of  $-u'v'$  occur near to and on either side of the contour  $D = 0$  on the  $R > 0$  branch of the  $(R, Q)$ -plane. Here  $u'$  and  $v'$  are the streamwise and wall-normal components of the velocity fluctuations respectively.

Chacin *et al.* (1996) found that the contributions to the Reynolds shear stress by an attached eddy come from regions close in physical space to the isosurface of  $D$ , which is small and positive as seen in figure 10 of that reference. They found that high Reynolds stress events are strongly correlated with changes in sign of the discriminant. This is important near the wall where the discriminant and the

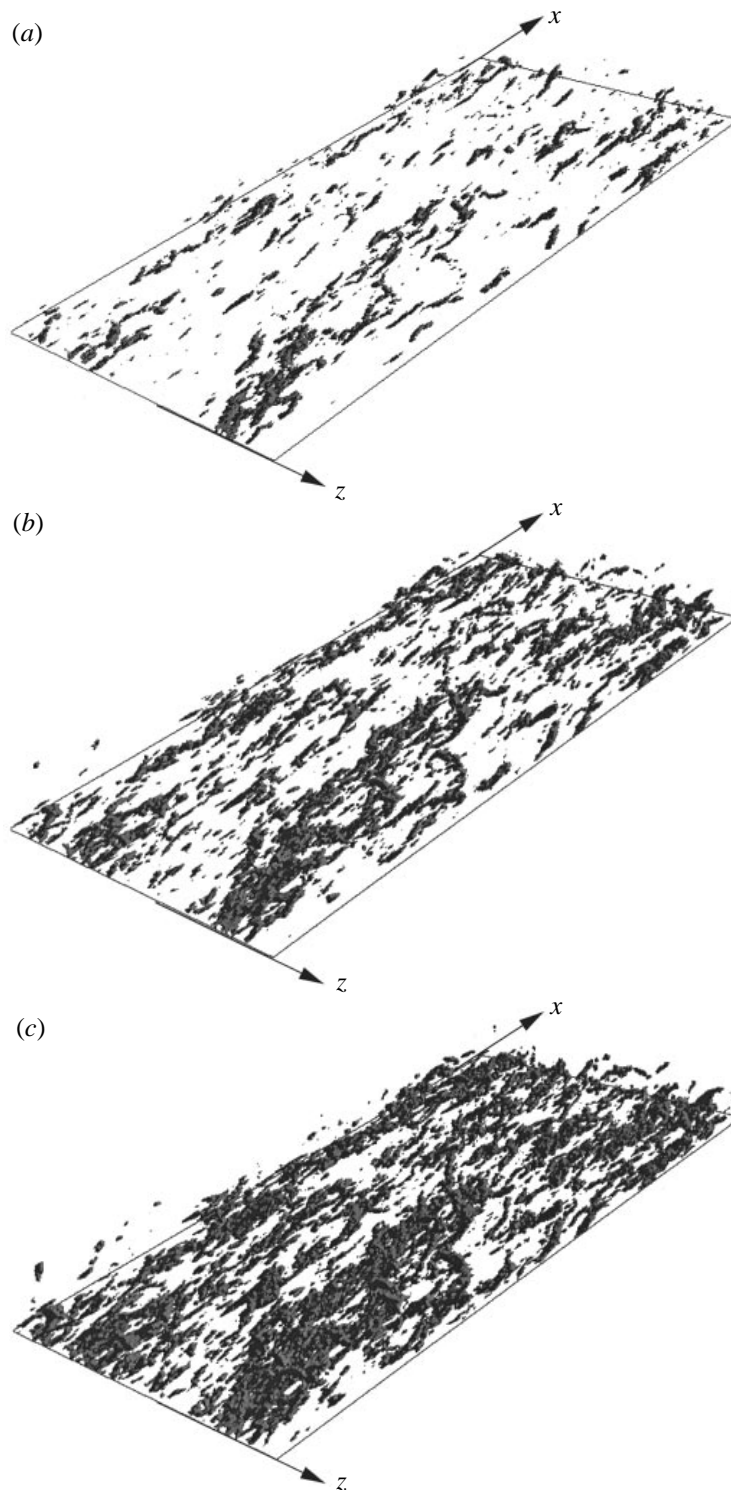


FIGURE 4. Isosurface of constant discriminant,  $D$ , for zero-pressure-gradient turbulent boundary layer flow at  $R_\theta = 670$  for the different threshold values of (a)  $D = 1.0$ , (b)  $D = 0.25$  and (c)  $D = 0.1$ . The displayed boundary layer structures cover  $\Delta x^+ = 2442$ ,  $y_{min}^+ = 6.4$ ,  $y_{max}^+ = 375$  and  $\Delta z^+ = 1221$ . Here  $^+$  denotes viscous lengths.



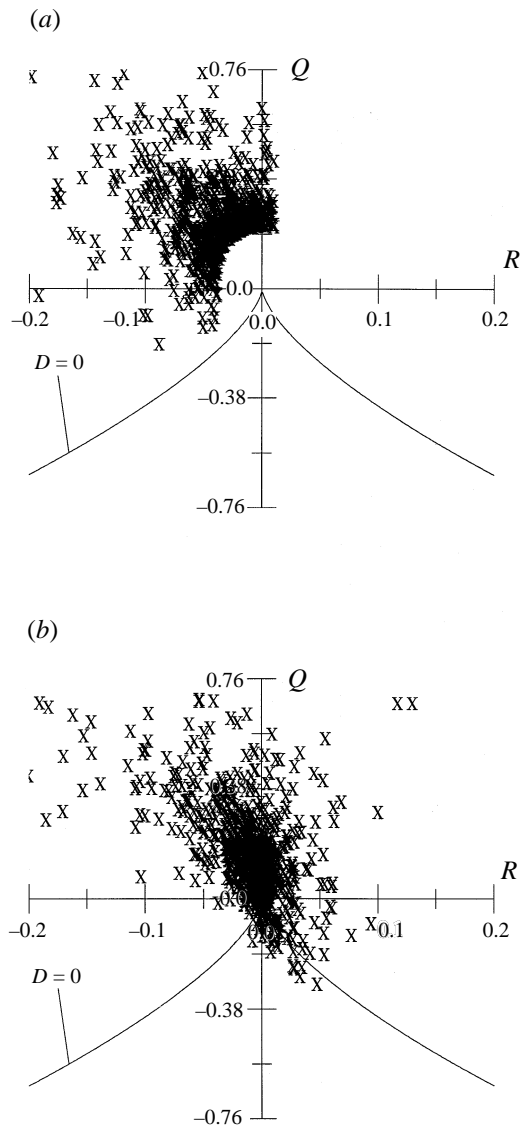
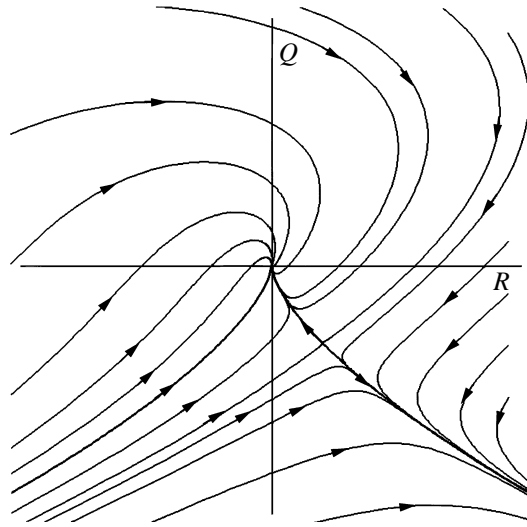


FIGURE 5. Particle migration on the  $(R, Q)$ -plane computed from the zero-pressure-gradient turbulent boundary layer data of Spalart (1988).

vorticity have a completely different character. The role of the discriminant needs to be clarified. One approach would be to analyse the velocity gradient tensor induced by artificial isolated eddies of various shapes using the Biot–Savart law in the manner of Perry & Marusic (1995).

Figures 9–12 show joint probability distribution diagrams of the various topological invariants. Figure 9 shows the joint p.d.f.'s of  $R$  and  $Q$  with figures 9(a–d) showing the results for the sublayer, buffer zone, logarithmic region, and wake region respectively. All the joint p.d.f.'s have a similar tear-drop shape around the origin with the contour levels shown on a logarithmic scale. The joint p.d.f. in the buffer layer has the largest extent in the  $(R, Q)$ -plane for a given contour, indicating that the velocity gradients attain their largest values within this region of the turbulent boundary layer. The

FIGURE 6. Particle trajectories using a linear diffusion model for  $H_{ij}$  of Martin & Dopazo (1995).

most significant effect in going from the viscous sublayer to the buffer region is a three-fold increase in maximum value of  $|Q|$  for  $Q > 0$  as a result of a significant increase in  $Q_w$  or enstrophy in some regions without a compensating increase of  $Q_s$ . This result is supported by the joint p.d.f. data between  $Q_w$  and  $Q_s$  shown in figure 11(a, b). The increase in  $|Q|$  for  $Q < 0$  is not quite as large, being a factor of 1.5. The extent of increase in  $|R|$  is of the same order for  $R < 0$  and  $R > 0$ . In the logarithmic region, the magnitude of the velocity gradient has decreased compared to the buffer layer. However, the shapes appear to be self-similar from the buffer zone onwards.

Figure 10 shows the joint p.d.f. of the invariants of the rate-of-strain tensor  $R_s$  and  $Q_s$ . In the sublayer, figure 10(a) shows that most of the rate of strain is two-dimensional, since the data collect along the  $Q_s$  axis and very high  $-Q_s$  values are encountered. This indicates that, locally, the highest dissipation of kinetic energy per unit mass occurs in the viscous sublayer and is produced by motions which are essentially two-dimensional. In the buffer zone results shown in figure 10(b) there is a drift towards  $D_s = 0$ , and the maximum value of  $|Q_s|$  has reduced to half that of the sublayer. Here  $D_s$  is the discriminant of the rate-of-strain tensor. In the buffer zone a large number of points in the flow have moved towards the origin of the  $(R_s, Q_s)$ -plane. In figure 10(c), the logarithmic region, there is a further decrease in the maximum value of  $|Q_s|$  and further movement of the joint p.d.f. towards the  $D_s = 0$  line. In this region the joint p.d.f. between  $R_s$  and  $Q_s$  has taken on the shape which is characteristic of a number of other turbulent flows including mixing layers (Soria *et al.* 1994), wakes (Soria & Chong 1993), and channel flow (Blackburn *et al.* 1996). The rate of strain is highly three-dimensional in the logarithmic region. In the wake region shown in figure 10(d), the maximum value of  $|Q_s|$  is orders of magnitude smaller than the other regions, which implies that very little dissipation is occurring there. The shape of the joint p.d.f. in the wake region is similar to that in the logarithmic region but with its extent reduced in the  $(R_s, Q_s)$ -domain.

Figure 11 shows the joint p.d.f.'s between  $-Q_s$  and  $Q_w$ . A line of  $45^\circ$  through the origin is symptomatic of vortex sheet behaviour or two-dimensional shearing provided  $R = 0$ . Data running close to the  $Q_w$ -axis could be interpreted as belonging to vortex

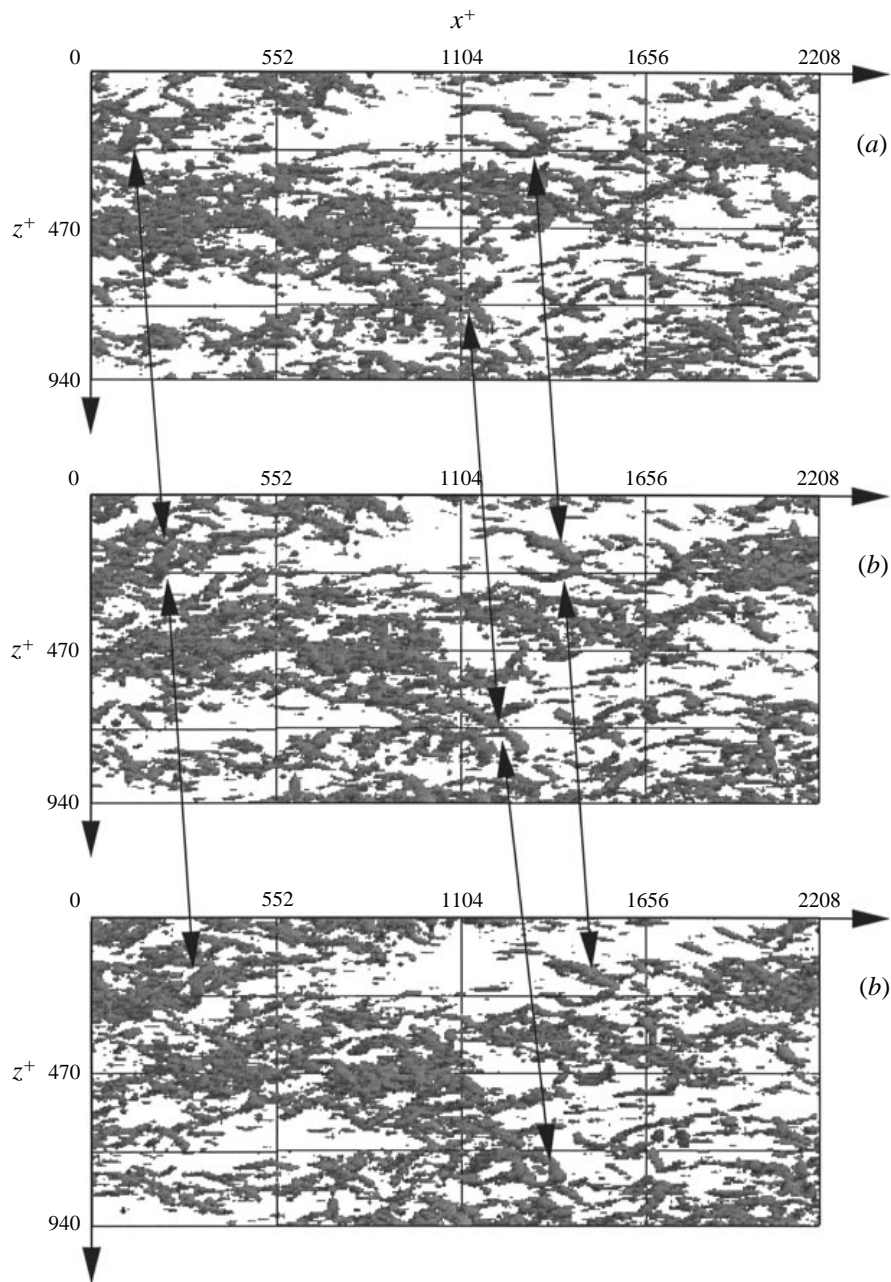


FIGURE 7. Three frames of a movie showing structures convecting downstream. Isosurfaces of discriminant ( $D \approx 0$ ) for zero-pressure-gradient data of Spalart for  $Re_\theta = 670$ . The time ( $tU_\infty/\delta^*$ ) sequence is: (a) 0, (b) 2.1 and (c) 3.9. This spans just over one eddy turnover time.

tubes, and data close to the  $-Q_s$ -axis correspond to irrotational rates of strain (Perry & Chong 1994). In figure 11(a) the sublayer results show a sheet-like behaviour, which is not surprising. All regions of the flow in the viscous sublayer have an approximate balance between  $Q_w$  and  $-Q_s$  which in turn implies that most of the regions of the flow have a  $Q$  value of approximately zero in the viscous sublayer as illustrated in

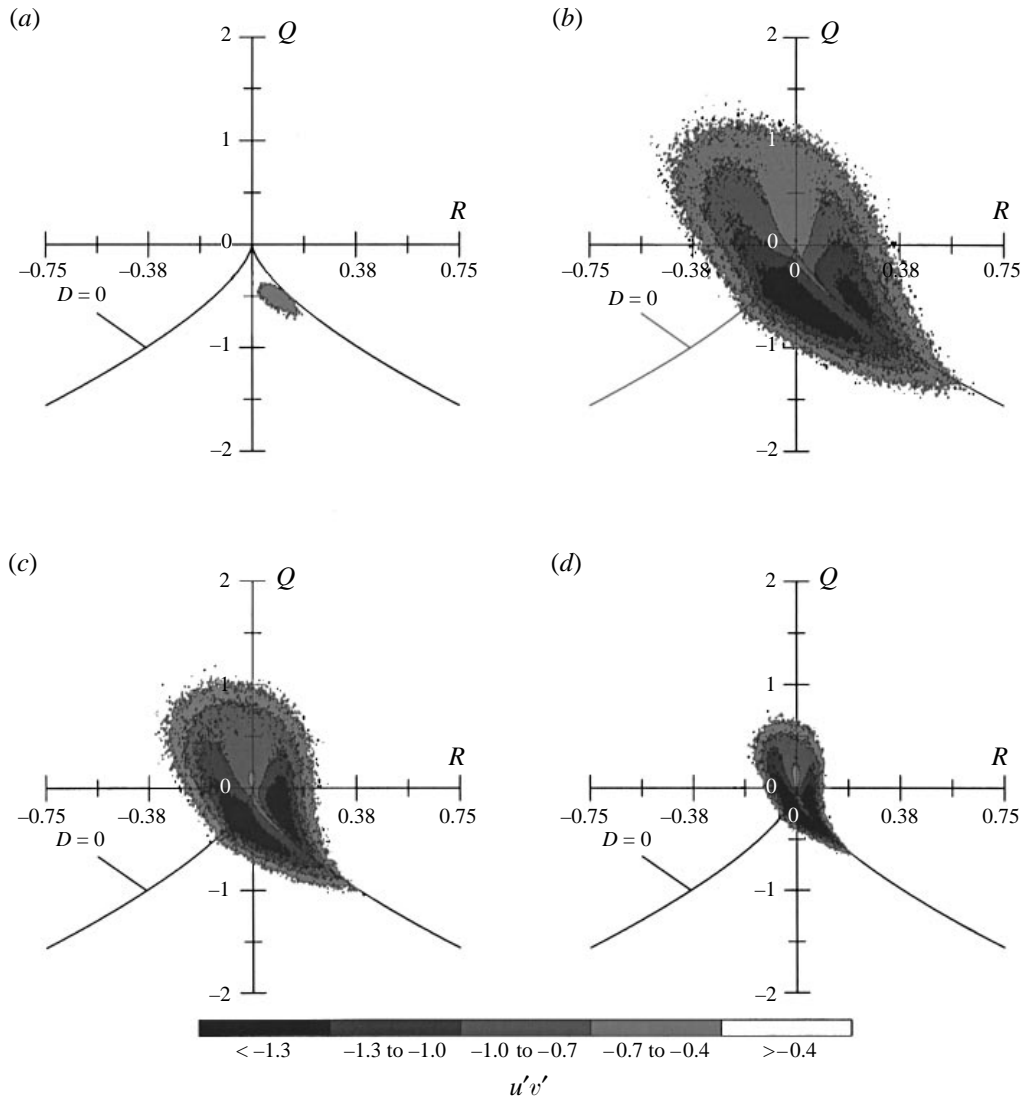


FIGURE 8. Time-averaged values of  $-u'v'$  for zero-pressure-gradient turbulent boundary layer flow with  $Re_\theta = 670$  in (a) viscous sublayer  $y^+ < 5.0$  (b) buffer layer,  $5.0 < y^+ < 41$ , (c) logarithmic region,  $41 < y^+ < 107$  and (d) wake region,  $y^+ > 107$ . The contour levels shown are normalized by  $u_\tau^2$ .

figure 9(a). In figure 11(b), the buffer zone results are shown and there is a mixture of various types of motions, but vortex sheet behaviour is still apparent. However, a noticeable increase in the regions with  $Q_w > -Q_s$  is observed in the buffer layer as a result of the vorticity being aligned with the strain field in such a way that a net stretching of vorticity occurs as indicated in the joint p.d.f. data of figure 12(b) to be discussed later. Although there is also an increase in the regions of the flow in the buffer layer in which  $-Q_s > Q_w$ , this effect is not as pronounced. Figure 11(c) shows a complete mixture of motion types and so also does figure 11(d). Of note in the logarithmic region is that the data in figure 11(c) show that regions with large values of  $Q_w$  range from regions with very small values of  $-Q_s$  to regions with  $Q_w \approx -Q_s$ .

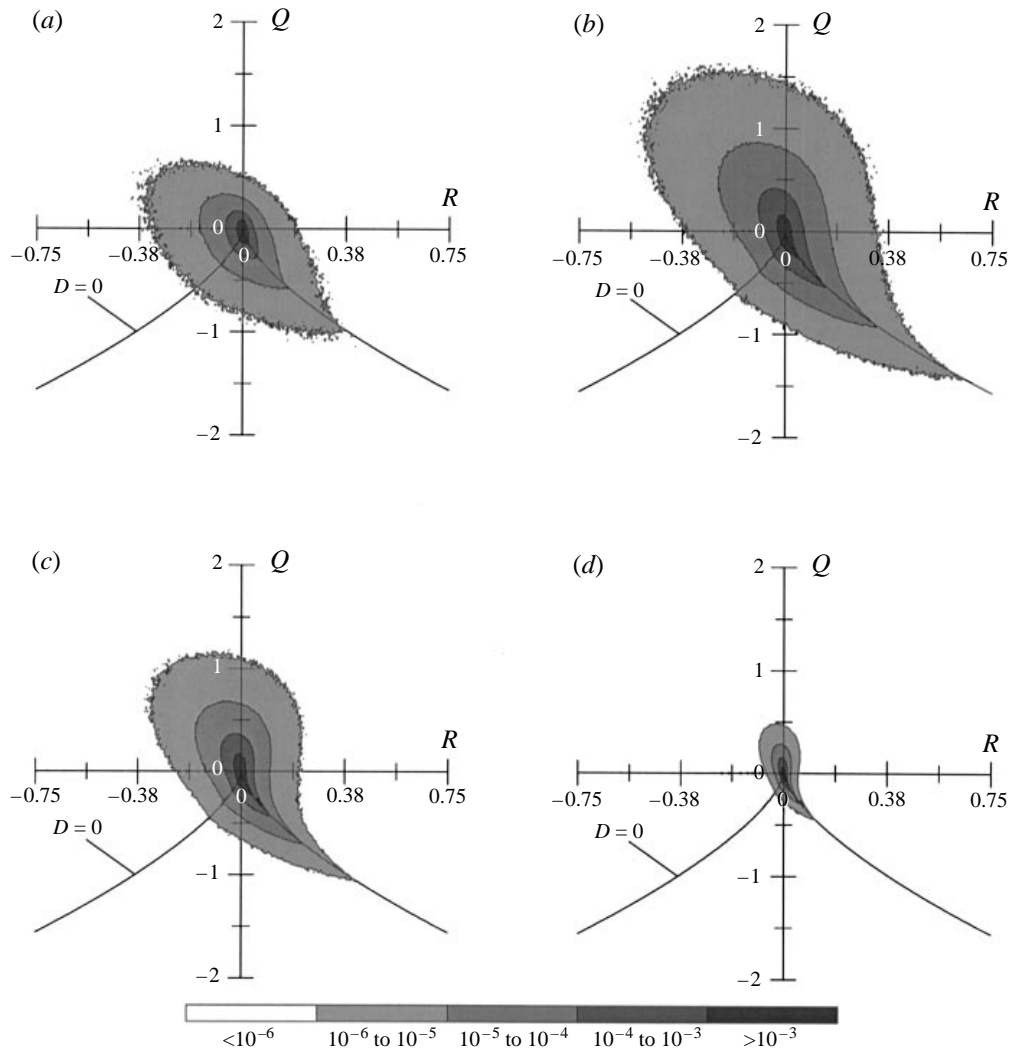


FIGURE 9. Joint probability density function between  $Q$  and  $R$  for zero-pressure-gradient turbulent boundary layer flow with  $R_\theta = 670$  in (a) viscous sublayer  $y^+ < 5.0$  (b) buffer layer,  $5.0 < y^+ < 41$ , (c) logarithmic region,  $41 < y^+ < 107$  and (d) wake region,  $y^+ > 107$ .

There is a tendency for the peak value of  $Q_w$  to be larger than the peak value of  $-Q_s$ . This is more pronounced in the wake region where the peak value of  $Q_w$  is nearly 50% higher than the peak value of  $-Q_s$  as shown in figure 11(d). The data also show that the regions of the wake domain of the boundary layer containing the peak  $Q_w$  value have a relatively low value of  $-Q_s$ , whereas the peak  $-Q_s$  regions are associated with motions which range from irrotational to vortical with  $Q_w \approx -Q_s$ . Although most of the results presented in figures 9–11 are consistent with the results of Blackburn *et al.* (1996), the latter two presented in figures 11(c, d) differ. In the turbulent channel flow investigated by Blackburn *et al.* (1996), the peak values of  $-Q_s$  are found to be larger than the peak values of  $Q_w$  both in the logarithmic and wake regions. This would tend to suggest a difference between these wall-bounded flows indicating that vortical structures with less mechanical dissipation and which

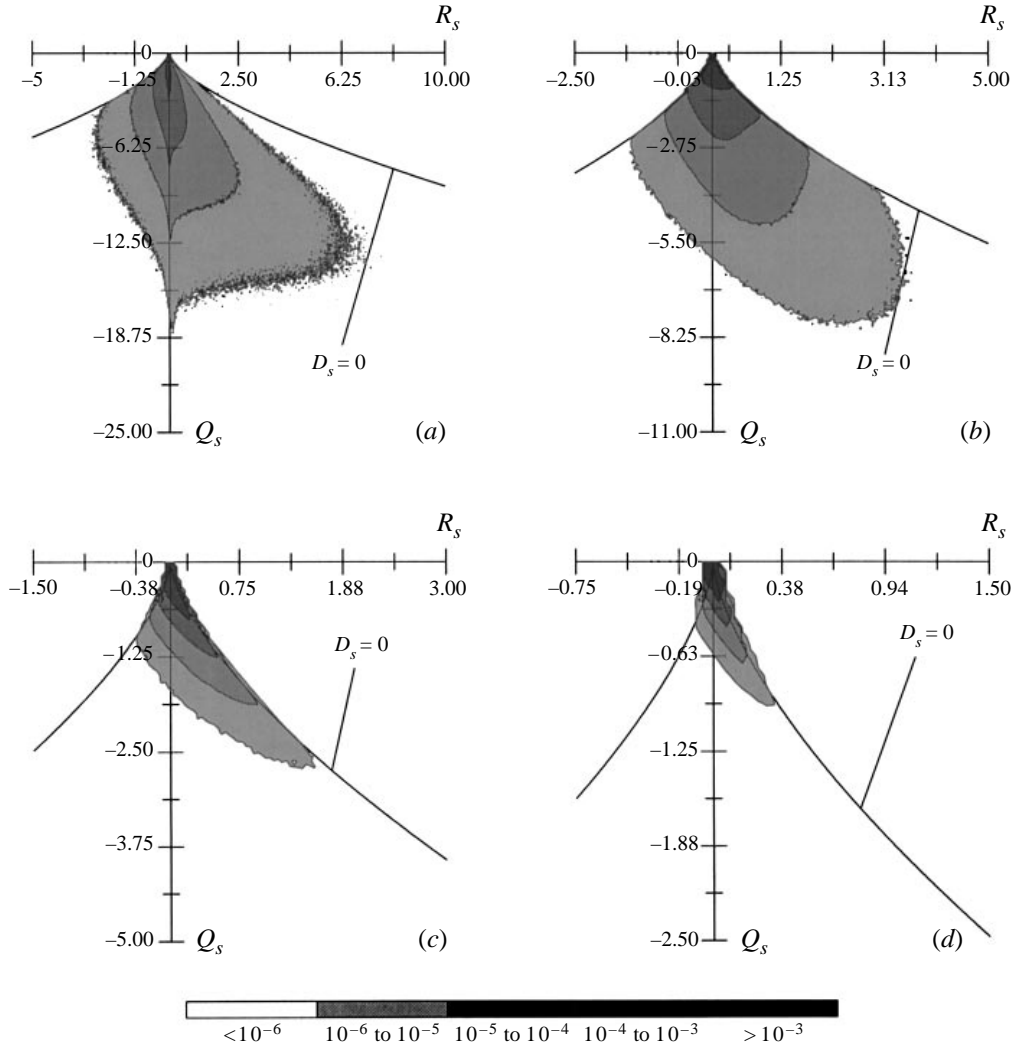


FIGURE 10. Joint probability density function between  $Q_s$  and  $R_s$  for zero-pressure-gradient turbulent boundary layer flow with  $R_\theta = 670$  in (a) viscous sublayer  $y^+ < 5.0$  (b) buffer layer,  $5.0 < y^+ < 41$ , (c) logarithmic region,  $41 < y^+ < 107$  and (d) wake region,  $y^+ > 107$ .

are therefore longer lived are present in the outer layers of the turbulent boundary layer which are not present in the channel flow.

The component of the strain field strength,  $-Q_s$ , which can amplify or reduce vorticity has been investigated using the joint p.d.f. between  $|\sigma|\sigma/2$  and  $Q_w$ . Here

$$\sigma = \frac{\omega_i S_{ij} \omega_j}{\omega_k \omega_k}, \quad (18)$$

where  $\omega_i$  is the vorticity vector. Also it can be shown (e.g. see Soria & Chong 1993) that

$$\omega_i S_{ij} \omega_j = 4(R_s - R). \quad (19)$$

The quantity  $|\sigma|\sigma/2$  is a measure of the stretching or contracting in the direction of the vorticity vector. Figure 12 shows the p.d.f.'s for the different domains of

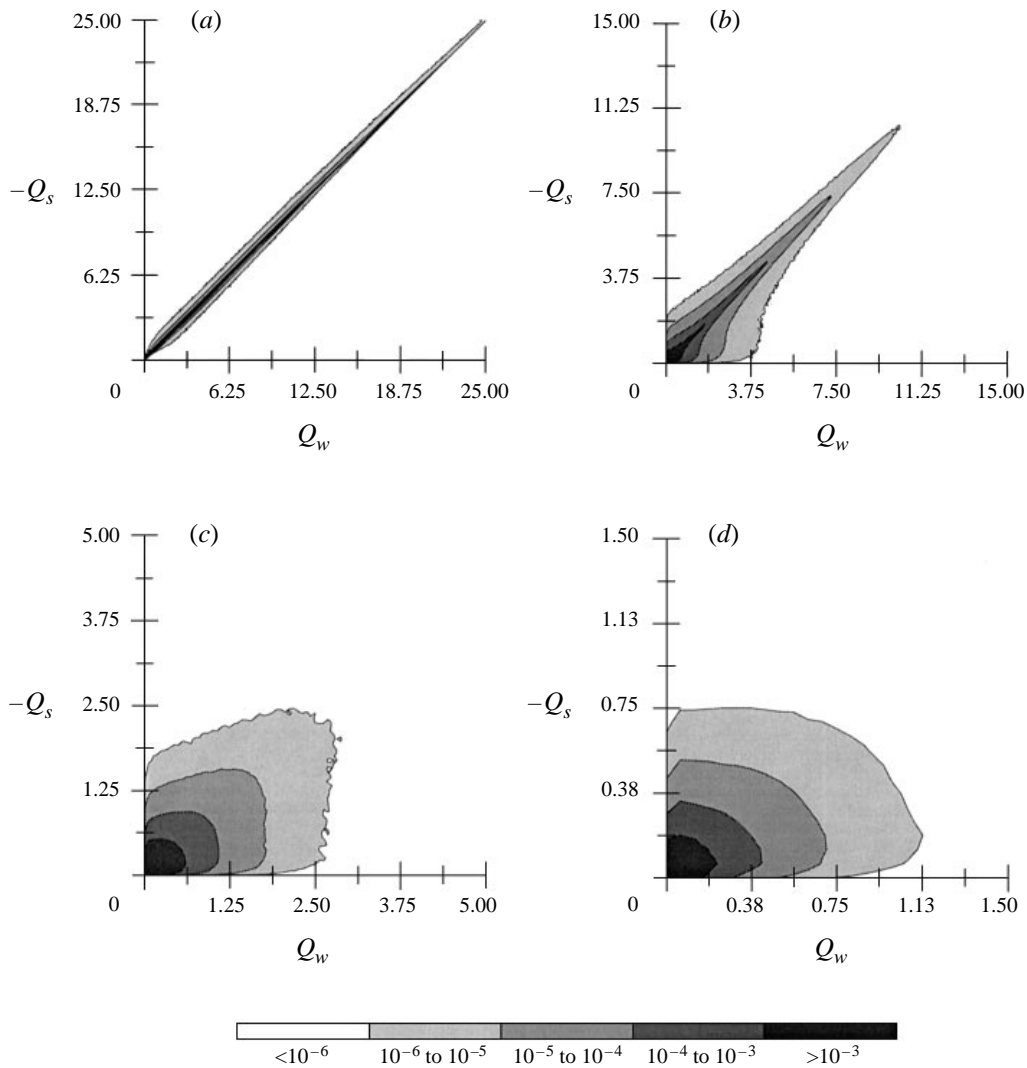


FIGURE 11. Joint probability density function between  $Q_w$  and  $-Q_s$  for zero-pressure-gradient turbulent boundary layer flow with  $R_\theta = 670$  in (a) viscous sublayer  $y^+ < 5.0$  (b) buffer layer,  $5.0 < y^+ < 41$ , (c) logarithmic region,  $41 < y^+ < 107$  and (d) wake region,  $y^+ > 107$ .

interest in the turbulent boundary layer. Interestingly, in all cases shown in figure 12 the highest vorticity has no stretching. In the viscous sublayer there are as many points where the vorticity is being stretched as there are points where the vorticity is being contracted. This picture changes markedly in the buffer layer where the peak stretching of vorticity has increased somewhat uniformly for regions with low to 0.5 of peak  $Q_w$  values. This has resulted in an increase of regions in which  $Q_w > -Q_s$  as indicated figure 12(b). The peak vorticity contraction has also increased by a factor of 2 in the buffer layer. However, this increase is present in regions of the buffer layer in which the vorticity is already inherently low and hence does not contribute to reducing the peak  $Q_w$  regions in the buffer layer. In the logarithmic region and the wake region the stretching or contracting in the direction of vorticity reduces

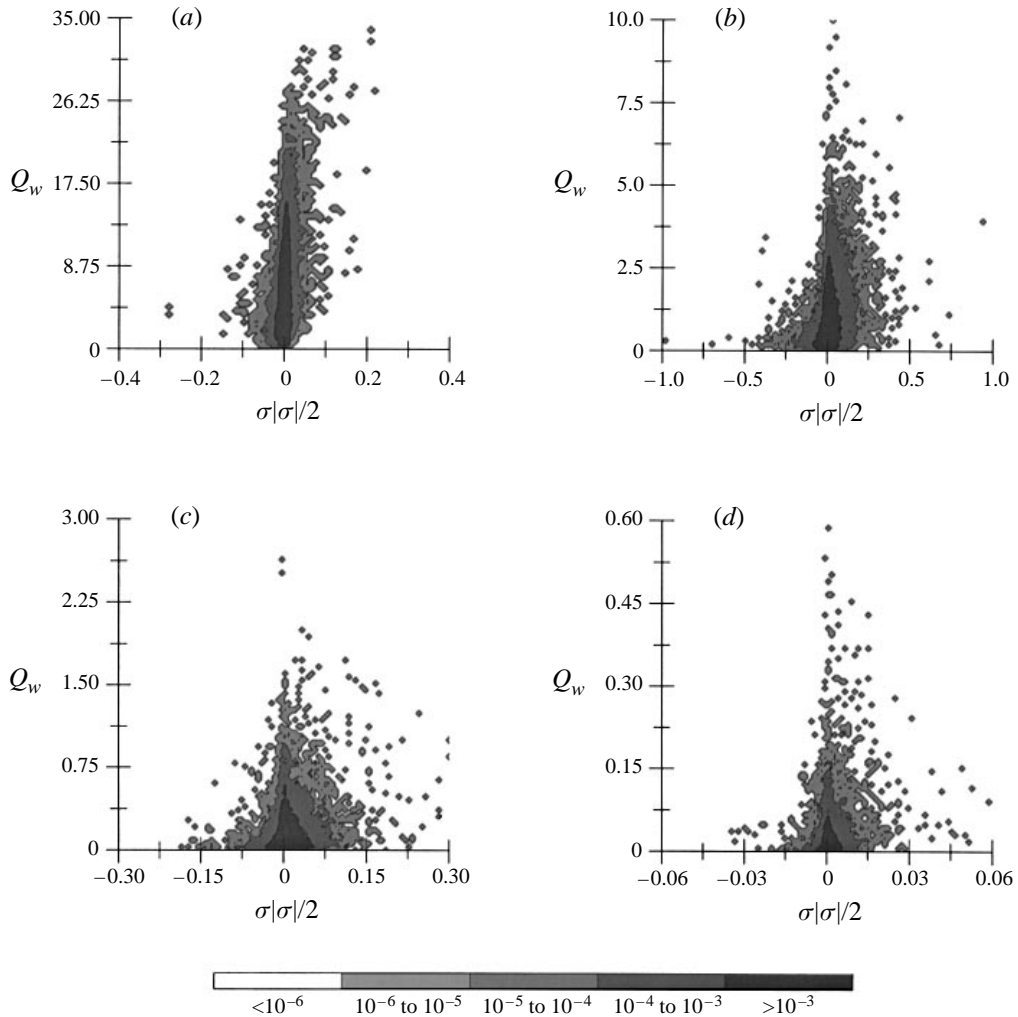


FIGURE 12. Joint probability density function between  $|\sigma|\sigma/2$  and  $Q_w$  for zero-pressure-gradient turbulent boundary layer flow with  $R_\theta = 670$  in (a) viscous sublayer  $y^+ = 1.2$  (b) buffer layer,  $y^+ = 16$ , (c) logarithmic region,  $y^+ = 87$  and (d) wake region,  $y^+ = 243$ .

continually as do the peak  $Q_w$  values in their respective joint p.d.f. As shown in figure 12(c,d) in both regions of the turbulent boundary layer there is a tendency for stretching of vorticity to predominate over contraction of vorticity. These results are qualitatively consistent with other inhomogeneous turbulent flow calculations such as the turbulent plane wake of Soria & Chong (1993).

Figure 13 shows the conditional-volume-integrated  $Q_w$  and  $Q_s$  for  $D$  greater than a specified threshold value as a function of this threshold value of  $D$ . These volume integrals have been normalized by the total volume integral of  $Q_w$  and  $Q_s$  respectively. In addition to the cases including the viscous zone, these normalized conditional integrals have been computed for  $y^+ > 6.4$ , thus eliminating the viscous sublayer contribution, and for  $y^+ > 37.4$ , thus eliminating the entire viscous zone contribution. The results show that independent of the  $y^+$  threshold, focal regions account for approximately 75% of all volume-integrated  $Q_w$  (i.e. enstrophy) and 66% of all volume-integrated  $Q_s$  (i.e. dissipation of mechanical energy).



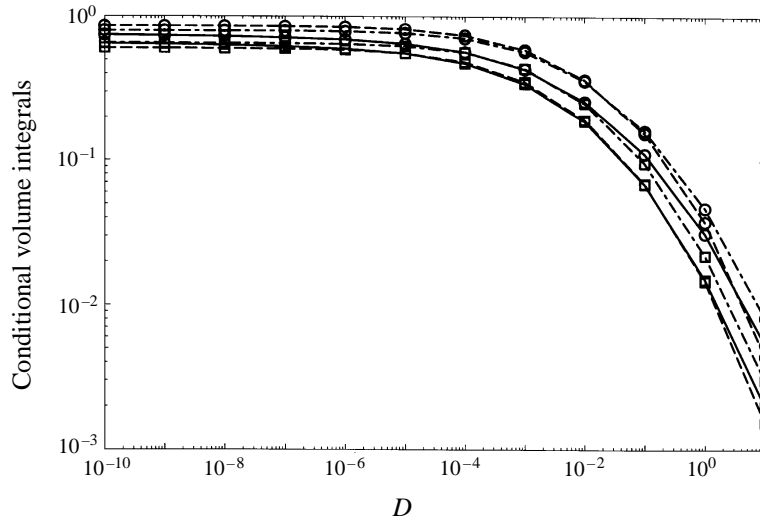


FIGURE 13. Conditional volume integrals of  $Q_s$  and  $Q_w$  normalized by the volume integrals of  $Q_s$  and  $Q_w$  respectively as a function of the cut-off value of the discriminant ( $D$ ).

- $\int Q_s(D > D_{given})dV / \int Q_s dV$ .
- $\int Q_w(D > D_{given})dV / \int Q_w dV$ .
- $\int Q_s(D > D_{given})dV / \int Q_s dV$  and  $y^+ > 6.4$
- $\int Q_w(D > D_{given})dV / \int Q_w dV$  and  $y^+ > 6.4$
- $\int Q_s(D > D_{given})dV / \int Q_s dV$  and  $y^+ > 37.4$
- $\int Q_w(D > D_{given})dV / \int Q_w dV$  and  $y^+ > 37.4$

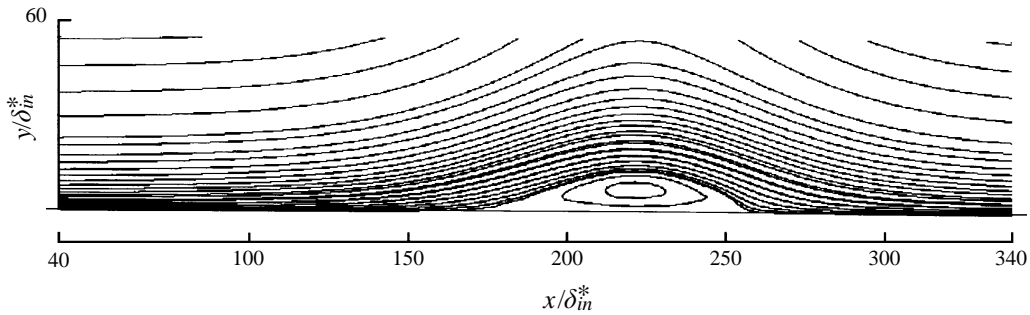
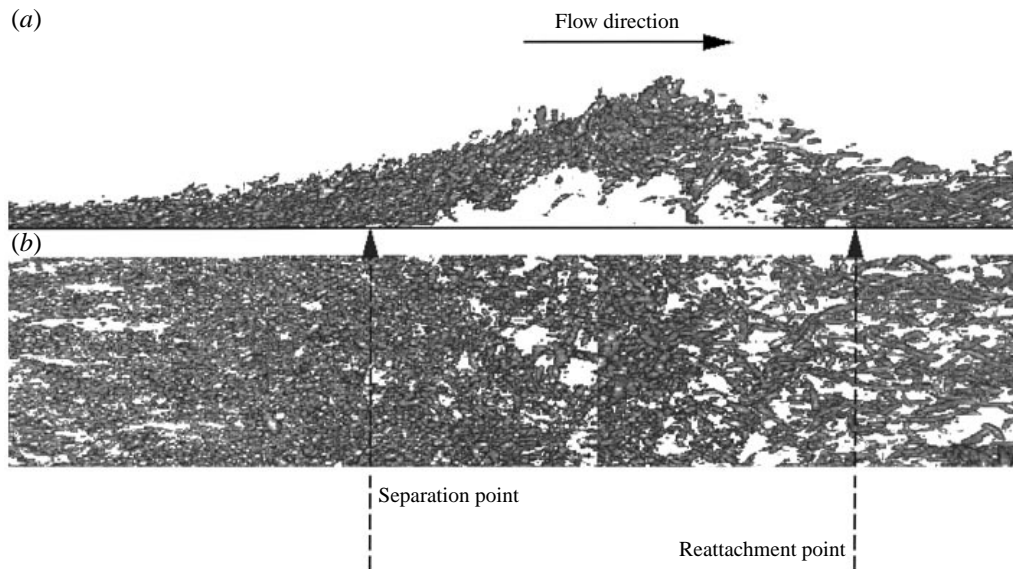


FIGURE 14. Mean streamline pattern for a turbulent boundary layer with separation and reattachment.

### 2.3. Separating and reattaching boundary layer

Figure 14 shows the mean flow streamlines of a turbulent boundary layer which nominally starts as a zero-pressure-gradient layer using the Spalart data of  $R_\theta = 330$  as an inflow boundary condition. These computations were carried out using a finite differences method and further details can be found in Na & Moin (1996). As the flow moves downstream, the pressure gradient is arranged to be zero, then adverse, and then favourable, resulting in a separation bubble. The flow bears a strong resemblance to the experiment of Perry & Fairlie (1975), but the Reynolds number for that experiment was orders of magnitude higher than this computation.

Figure 15(a) shows an elevation view of the isosurfaces of the discriminant, and one can see a myriad of structures, many of which extend through from the wall to

FIGURE 15 (*a,b*). For caption see facing page.

the outer edge of the boundary layer and generally lean in the streamwise direction. The structures leave the wall completely downstream of the mean separation point and ride over the separation bubble and then reattach. In the separation bubble there is an extensive region which seems to be devoid of fluid particles with positive discriminant. Figure 16(*a*) shows the instantaneous surface limiting streamlines or 'skin friction lines'. In the upstream part of the flow, bifurcation lines (curves towards which neighbouring trajectories asymptote) are most evident. The precise definition and properties of such lines are given by Hornung & Perry (1984) and Perry & Hornung (1984). As the pressure gradient becomes adverse, the skin friction lines reveal critical points all over the surface prior to the mean flow separation region. This means that there exist momentarily small-scale flow reversals scattered over the region prior to the large-scale mean separation bubble. Under the bubble, the scale or spacing of the critical points is much larger than in the mean attached flow and large nodes of separation and reattachment are evident near the mean flow separation and reattachment 'lines' respectively. After reattachment, bifurcation lines are re-formed after a short streamwise distance with a much wider spanwise spacing than upstream of the separation bubble. This spacing is no doubt related to the viscous scaling as a lower shear velocity gives rise to the wider spacing.

Figure 16(*b*) shows the surface vortex lines which are orthogonal to the skin friction lines. In regions far upstream and downstream of the separation bubble, kinks in the vortex lines indicate a bifurcation line in the skin friction lines. Hornung & Perry (1984) showed that near a bifurcation line, neighbouring skin friction lines are exponential curves and the vortex lines are orthogonal parabolas. Figure 17 shows skin-friction lines and vortex lines superimposed for selected parts of the flow and the bifurcation patterns just mentioned are apparent. This orthogonality property throughout the limiting wall field acts as a useful check on the correctness of our data processing and of some aspects of the computations. Critical points in the limiting surface streamlines are also critical points in vorticity. In the separation region, the large velocity field nodes which are apparent are foci in the vorticity field.

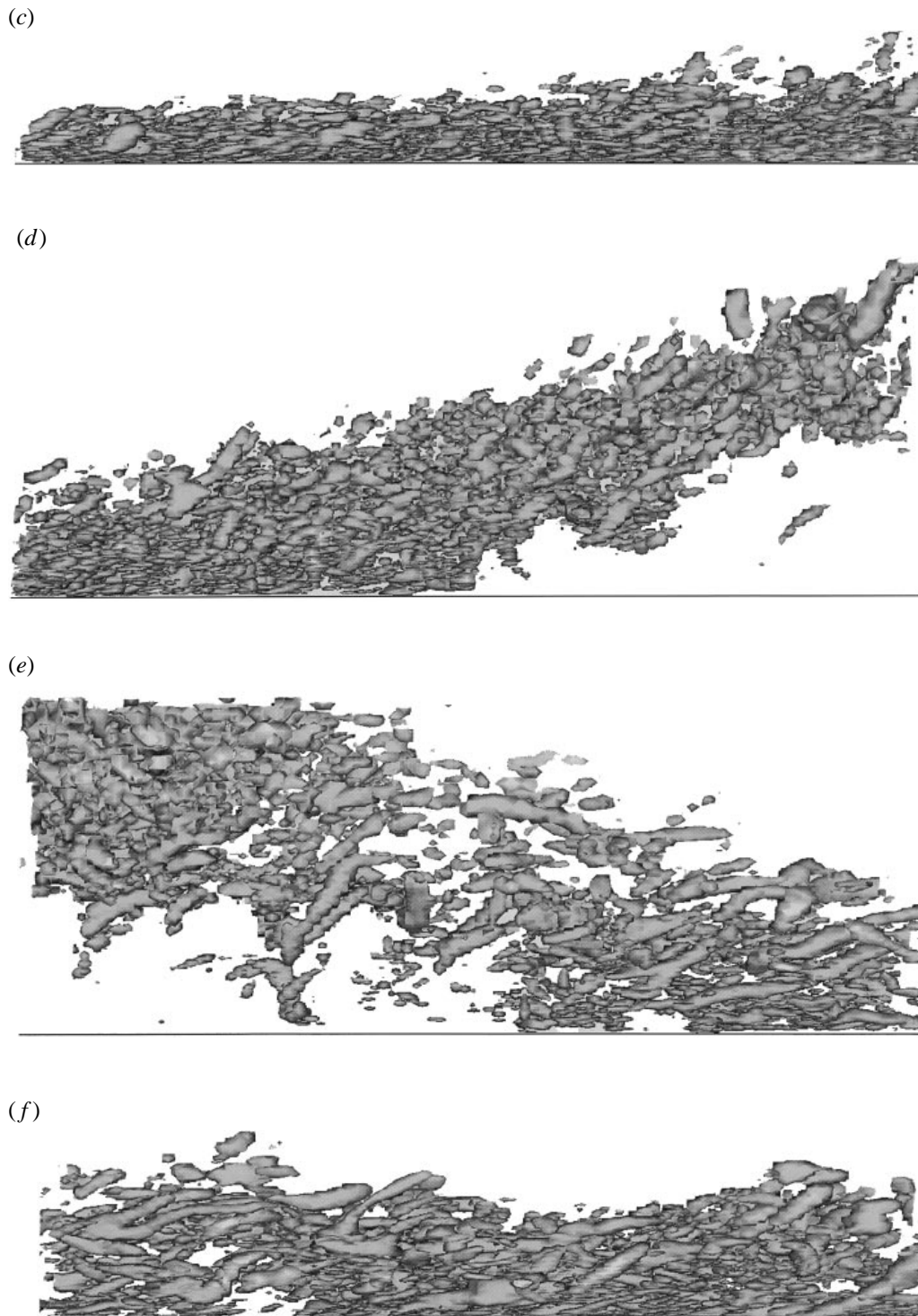


FIGURE 15. Isosurfaces of constant  $D \sim 1$  to 10 showing focal structures in a turbulent boundary layer with separation and reattachment from  $x/\delta_m^* \approx 90$  to  $x/\delta_m^* \approx 300$ . (a) Elevation views. (b) Plan views. (c–f) Enlarged views of (a) in going from left to right.

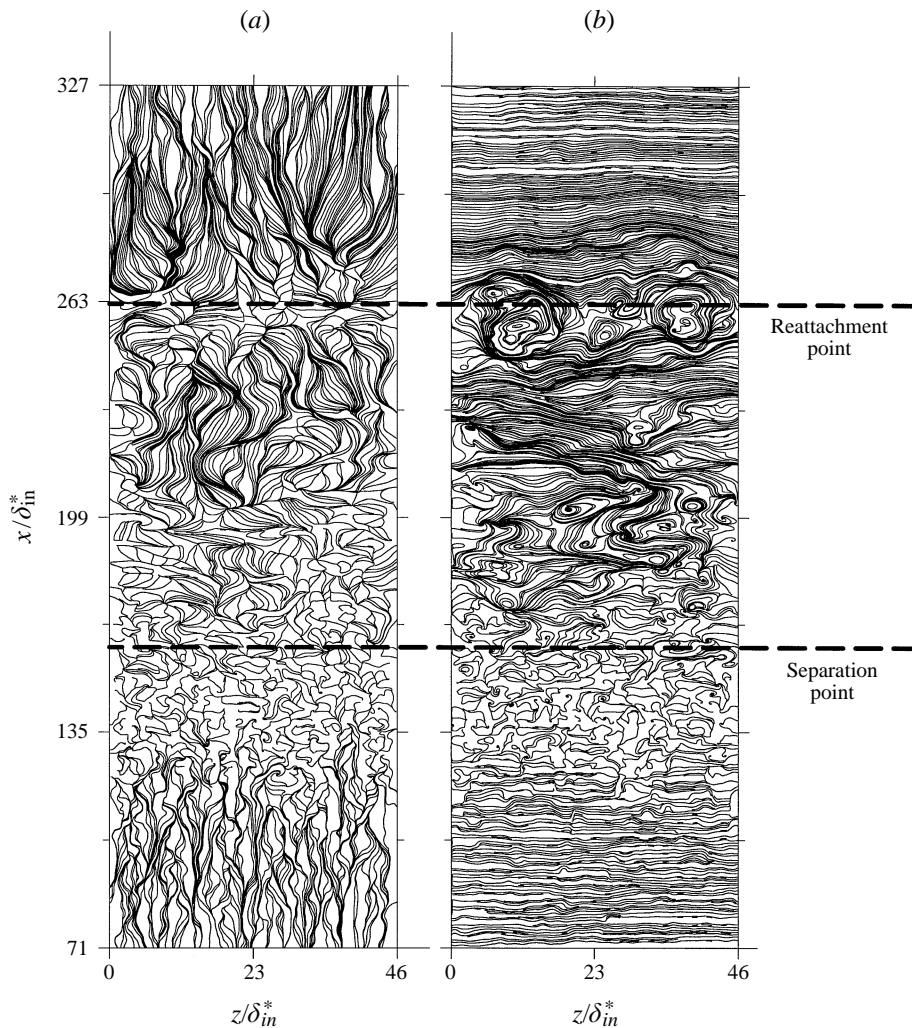


FIGURE 16. (a) Skin-friction lines and (b) surface vorticity lines from  $x/\delta_m^* \approx 90$  to  $x/\delta_m^* \approx 300$ .

In figure 15, the side and plan views of the isosurfaces of the discriminant show that the structures appear to be pulled apart and stretched as they ride over the separation bubble. Coles (1956, 1957) formulated a hypothesis for the mean velocity profiles which considers a turbulent boundary layer to consist of two components superimposed – namely a wall component which follows the universal law of the wall and a wake component which follow a universal law of the wake. Recently this has been extended to include the turbulence structure by Perry & Marusic (1995) and Marusic & Perry (1995) where the wall component for both mean flow and Reynolds stress is considered to be generated by wall attached eddies where the vortex lines connect to the wall like the Theodorsen-type eddies as shown sketched in figure 18(a). The wake component of velocity and the peak in the Reynolds shear stress which occurs well away from the wall when the Coles wake factor is appreciable are considered to be generated by wake eddies which are thought to consist of spanwise undulating vortex cores as shown in figure 18(b). This model is supported by mean flow, broadband turbulence and spectral measurements and an analysis



FIGURE 17. Skin-friction lines and surface vorticity lines superimposed. (a) Unseparated region. (b) Separated region.

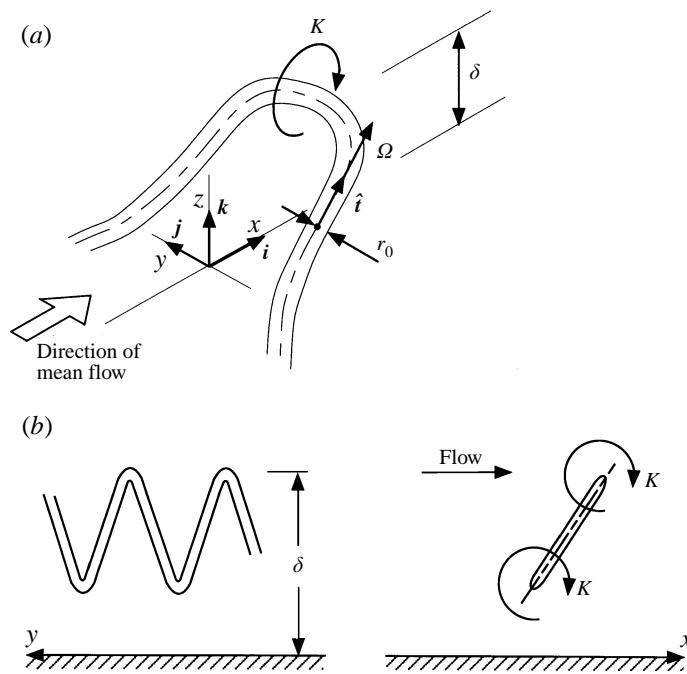


FIGURE 18. (a) Wall eddies and (b) wake eddies, after Perry & Marusic (1995). Note that here, unlike earlier convention,  $z$  is the coordinate normal to the wall rather than  $y$ ;  $x$  is the streamwise direction;  $K$  is circulation,  $r_0$  is the size of the vortex core,  $\Omega$  is vorticity and  $\delta$  is the height of the eddy from the wall.

using convolution integrals for computing the effect of a random array of eddies with a range of scales (see Perry & Marusic 1995 for details). It is almost obvious from the picture of the isosurface of the discriminant in figure 15 that as the flow develops in the adverse pressure gradient and as the Coles wake factor increases, more of the eddies which contribute to the Reynolds shear stress and mean flow vorticity are eddies which are not connected to the wall. Once separation has occurred, there are no eddies connected with the wall. Unfortunately, memory limitations of the flow visualization software prevented a full rendering of the details of the flow field, causing the isosurfaces to appear lumpy and unstructured.

### 3. Conclusions

This study has shown that structures carrying Reynolds shear stress in zero-pressure-gradient layers consist of attached vortex loops of the type envisaged by Theodorsen (1955), Perry & Chong (1982) and others. These structures form vortex tubes or arches of positive discriminant of the velocity gradient tensor. The evidence presented here indicates that Reynolds stress generation is correlated with a change in sign of the discriminant of the velocity gradient tensor.

For adverse-pressure-gradient layers, there is encouraging evidence of structures carrying Reynolds shear stress which are not connected to the wall and that there is a combination of wall and wake structures as suggested by the work of Perry & Marusic (1995).

This work was supported by the Centre for Turbulence Research, NASA AMES–Stanford Joint Institute for Aeronautics and Acoustics, NASA Grant NAG-1-1610 and the Australian Research Council. Partial support was provided by the NASA–Ames Joint Institute for Aeronautics and Acoustics Grant NCC 2-55. Additional supercomputing resources were provided by the San Diego Supercomputer Centre.

### REFERENCES

- BLACKBURN, H. M., MANSOUR, N. N. & CANTWELL, B. J. 1996 Topology of fine-scale motions in turbulent channel flow. *J. Fluid Mech.* **310**, 269–292.
- CANTWELL, B. J. 1979 Coherent turbulent structures as critical points in unsteady flow. *Archiwum Mechaniki Stosowanej. (Archives of Mechanics)* **31**(5), 707–721.
- CANTWELL, B. J. 1992 Exact solution of a restricted Euler equation for the velocity gradient tensor. *Phys. Fluids* **4**, 782–793.
- CHACIN, J. M., CANTWELL, B. J. & KLINE, S. J. 1996 Study of turbulent boundary structure using the invariants of the velocity gradient tensor. *J. Expl. Thermal Fluid Sci.* **13**, 308–317.
- CHONG, M. S., PERRY, A. E. & CANTWELL, B. J. 1989 A general classification of three-dimensional flow fields. In *Proc. IUTAM Symp. on Topological Fluid Mechanics, Cambridge* (ed. H. K. Moffatt & A. Tsinober), pp. 408–420.
- CHONG, M. S., PERRY, A. E. & CANTWELL, B. J. 1990 A general classification of three-dimensional flow fields. *Phys. Fluids A* **4**, 765–777.
- DALLMANN, U. 1983 Topological structures of three-dimensional flow separations. *DFVLR Rep. IB 221-82-A07* Göttingen, West Germany.
- HEAD, M. R. & BANDYOPADHYAY, P. 1981 New aspects of turbulent structure. *J. Fluid Mech.* **107**, 297–337.
- HORNUNG, H. G. & PERRY, A. E. 1984 Some aspects of three-dimensional separation. Part I. Streamsurface bifurcations. *Z. Flugwiss. Weltraumforsch.* **8**, 7–87.
- JEONG, J. & HUSSAIN, F. 1995 On the identification of a vortex. *J. Fluid Mech.* **285**, 69–94.
- KIM, J. 1989 On the structure of pressure fluctuations in simulated turbulent channel flow. *J. Fluid Mech.* **205**, 421–451.

- LUGT, H. J. 1979 The dilemma of defining a vortex. In *Recent Developments in Theoretical and Experimental Fluid Mechanics* (ed. U. Muller, K. G. Roesner & B. Schmidt), pp. 309–321. Springer.
- MARTIN, J. & DOPAZO, C. 1995 Velocity gradient invariant evolution from a linear diffusion model. In *Proc. Twelfth Australasian Fluid Mechanics Conf.*, pp. 743–746.
- MARUSIC, I. & PERRY, A. E. 1995 A wall-wake model for the turbulent structure of boundary layers. Part 2. Further experimental support. *J. Fluid Mech.* **298**, 389–407.
- NA, Y. & MOIN, P. 1996 Direct numerical simulation of turbulent boundary layers with adverse pressure gradient and separation. *Stanford University Rep.* TF-68.
- PERRY, A. E. & ABELL, C. J. 1977 Asymptotic similarity of turbulent structures in smooth and rough-walled pipes. *J. Fluid Mech.* **79**, 785–799.
- PERRY, A. E. & CHONG, M. S. 1982 On the mechanism of wall turbulence. *J. Fluid Mech.* **119**, 173–217.
- PERRY, A. E. & CHONG, M. S. 1994 Topology of flow patterns in vortex motions and turbulence. *Appl. Sci. Res.* **54**(3/4), 357–374.
- PERRY, A. E. & FAIRLIE, B. D. 1975 A study of turbulent boundary-layer separation and reattachment. *J. Fluid Mech.* **69**, 657–672.
- PERRY, A. E., HENBEST, S. M. & CHONG, M. S. 1986 A theoretical and experimental study of wall turbulence. *J. Fluid Mech.* **165**, 163–199.
- PERRY, A. E. & HORNING, H. G. 1984 Some aspects of three-dimensional separation. Part II. Vortex skeletons. *Z. Flugwiss. Weltraumforsch.* **8**, 155–160.
- PERRY, A. E. & LI, J. D. 1990 Experimental support for the attached-eddy hypothesis in zero-pressure-gradient turbulent boundary layers. *J. Fluid Mech.* **218**, 405–438.
- PERRY, A. E., LI, J. D. & MARUSIC, I. 1991 Towards a closure scheme for turbulent boundary layers using the attached eddy hypothesis. *Phil. Trans. R. Soc. Lond. A* **336**, 67–79.
- PERRY, A. E., LIM, K. L. & HENBEST, S. M. 1987 An experimental study of the turbulence structure in smooth- and rough-wall boundary layers. *J. Fluid Mech.* **177**, 437–466.
- PERRY, A. E. & MARUSIC, I. 1995 A wall-wake model for the turbulent structure of boundary layers. Part 1. Extension of the attached eddy hypothesis. *J. Fluid Mech.* **298**, 361–388.
- PERRY, A. E., MARUSIC, I. & LI, J. D. 1994 Wall turbulence closure based on classical similarity laws and the attached eddy hypothesis. *Phys. Fluids* **2**, 1024–1035.
- ROBINSON, S. K. 1991 Coherent motions in the turbulent boundary layer. *Ann. Rev. Fluid Mech.* **23**, 601–639.
- SORIA, J. & CANTWELL, B. J. 1994 Topological visualisation of focal structures in free shear flows. *Appl. Sci. Res.* **53**, 375–386.
- SORIA, J. & CHONG, M. S. 1993 The structure of intense focal regions in a direct numerical wake flow calculation. In *Proc. Ninth Symp. on Turbulent Shear Flows*, pp. 3.1.1–3.1.6.
- SORIA, J., CHONG, M. S., SONDERGAARD, R., PERRY, A. E. & CANTWELL, B. J. 1992 Topology of time-developing incompressible mixing layers. In *Proc. Center for Turbulence Research Summer Program, 1992*, pp. 101–121. Stanford University/NASA Ames.
- SORIA, J., CHONG, M. S., SONDERGAARD, R., PERRY, A. E. & CANTWELL, B. J. 1994 A study of the fine scale motions of incompressible time-developing mixing layers. *Phys. Fluids* **6**, 871–884.
- SPALART, P. R. 1988 Direct simulation of a turbulent boundary layer up to  $Re_\theta = 1410$ . *J. Fluid Mech.* **187**, 61–98.
- THEODORSEN, T. 1955 *The Structure of Turbulence*. 50 Jahre Grenzschichtforschung.
- TOWNSEND, A. A. 1976 *The Structure of Turbulent Shear Flow*, 2nd edn. Cambridge University Press.
- TRUESDELL, C. 1954 *The Kinematics of Vorticity*. Indiana University Press.
- VIEILLEFOSSE, P. 1982 Local interaction between vorticity and shear in a perfect incompressible fluid. *J. Phys. (Paris)* **43**, 837–842.
- VIEILLEFOSSE, P. 1984 Internal motion of a small element of fluid in an inviscid flow. *Physica A* **150**, 150–162.
- VOLLMERS, H. 1983 Separation and vortical-type flow around a prolate spheroid. Evolution of relevant parameters. In *AGARD Symp. on Aerodyn. of Vortical Type Flow in Three-Dimensions Rotterdam, AGARD-CP342*, pp. 14.1–14.14.